Coastal Orographic Rainfall Processes Observed by Radar during the California Land-Falling Jets Experiment

ALLEN B. WHITE

Cooperative Institute for Research in Environmental Sciences, University of Colorado, and NOAA/Environmental Technology Laboratory, Boulder, Colorado

PAUL J. NEIMAN AND F. MARTIN RALPH

NOAA/Environmental Technology Laboratory, Boulder, Colorado

DAVID E. KINGSMILL

Desert Research Institute, Reno, Nevada

P. OLA G. PERSSON

Cooperative Institute for Research in Environmental Sciences, University of Colorado, and NOAA/Environmental Technology Laboratory, Boulder, Colorado

(Manuscript received 4 June 2002, in final form 26 September 2002)

ABSTRACT

Radar and rain gauge observations collected in coastal mountains during the California Land-Falling Jets Experiment (CALJET) are used to diagnose the bulk physical properties of rainfall during a wet winter season (January–March 1998). Three rainfall types were clearly distinguishable by differences in their vertical profiles of radar reflectivity and Doppler vertical velocity: nonbright band, bright band, and hybrid (seeder–feeder). The contribution of each rainfall type to the total rainfall observed at the radar site (1841 mm) was determined by a new, objective algorithm. While hybrid rain occurred most often, nonbrightband rain (NBB rain) contributed significantly (28%) to the total. This paper focuses on characterizing NBB rain because of the need to document this key physical process and because of its impact on Weather Surveillance Radar-1988 Doppler (WSR-88D) precipitation surveillance capabilities.

NBB rain is a quasi-steady, shallow rain process that does not exhibit a radar bright band, that occurs largely beneath the melting level, and that can produce rain rates exceeding 20 mm h^{-1}. Composite vertical profiles were produced for NBB rain using 1417 samples and brightband rain using 5061 samples. Although the mean rain rate for each composite was 3.95 mm h^{-1}, at all altitudes NBB rain had systematically weaker equivalent radar reflectivity (e.g., 20.5 dBZ_e vs 28.5 dBZ_e at 263 m above ground level) and much smaller Doppler vertical fall velocities (e.g., 2.25 m s^{-1} vs 6.25 m s^{-1} at 263 m) than did brightband rain. The reflectivity–rain-rate (Z–R) relationship for NBB rain ($Z = 1.2R^{1.8}$) differs significantly from that of brightband/hybrid rain ($Z = 207R^{1.1}$).

The meteorological context in which NBB rain occurred is described through case studies and seasonal statistics. NBB rain occurred in a wide variety of positions relative to frontal zones within land-falling storms, but three-quarters of it fell when the layer-mean, profiler-observed wind direction at 1250 m MSL (the altitude of the composite low-level jet) was between 190° and 220°. The importance of orographic forcing during NBB rain, relative to all rain events, was indicated by a stronger correlation between upslope wind speed and coastal rain rates at 1250 m MSL ($r = 0.74$ vs $r = 0.54$), stronger low-level wind speeds, and wind directions more orthogonal to the mean terrain orientation.

1. Introduction

The overarching goal of the California Land-Falling Jets Experiment (CALJET; Ralph et al. 1998) was to help improve the 0–24-h forecasts of damaging weather impacting the western United States, with a particular emphasis on the coast of California. This goal is being pursued further and expanded to other West Coast states through the ongoing efforts of the Pacific Land-Falling Jets Experiment (PACJET; for more information on PACJET, see http://www.etl.noaa.gov/programs/pacjet/). During CALJET, both ground-based and airborne platforms were used to obtain detailed measurements in storm environments across California's coastal domain and the

Corresponding author address: Dr. Allen B. White, NOAA/ETL, Mail Code R/ET7, 325 Broadway, Boulder, CO 80305.
E-mail: allen.b.white@noaa.gov

© 2003 American Meteorological Society

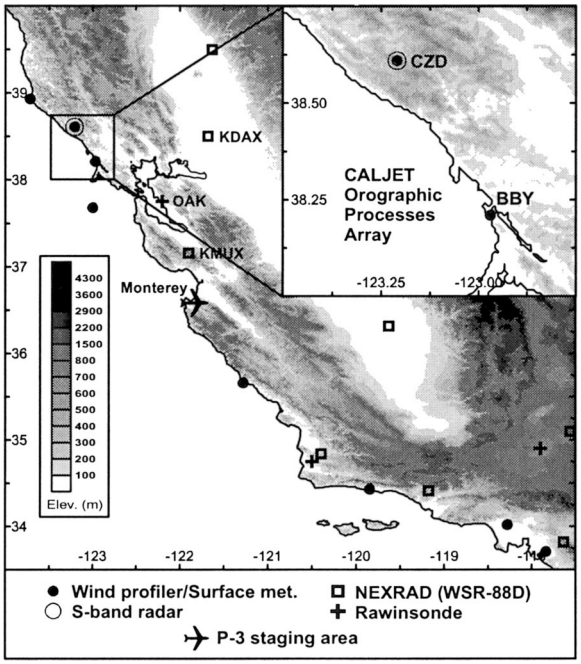

FIG. 1. Base map of California showing gray-shaded terrain (m) and the locations of the upper-air observing sites (see key) used during CALJET. The inset box highlights the CALJET orographic processes array, including the Cazadero (CZD) site that housed the vertically pointing S-band profiler, a 915-MHz wind profiler with RASS, a surface meteorological station, and a laser ceilometer. Each observing site discussed in the text is accompanied by its three- or four-letter station name.

data-sparse eastern Pacific Ocean (see Fig. 1). An orographic processes array was deployed within the larger CALJET network to study orographic precipitation enhancement in the climatologically flood-prone Russian River watershed. In this array, the National Oceanic and Atmospheric Administration's Environmental Technology Laboratory (NOAA/ETL) operated an S-band radar profiler (hereafter, S-PROF) at a coastal mountain site (labeled CZD in Fig. 1) above the town of Cazadero, California. This vertically pointing radar was designed with an extended dynamic-range capability to provide sensitivity to the more strongly reflecting regions of nonprecipitating clouds and to prevent receiver saturation in regions of high reflectivity, including the melting layer.

Improvements in quantitative precipitation forecasting for the coastal zone will depend on a better understanding of the microphysical processes associated with orographic precipitation. In this paper we identify and describe a quasi-steady, orographically forced, shallow rain process observed by S-PROF that contributed substantially to the total rainfall during CALJET and, yet, was mostly undetected by the operational network of the National Weather Service (NWS) Weather Surveillance Radar-1988 Doppler (WSR-88D). The Russian River watershed is not alone in experiencing this coverage problem. Gaps in WSR-88D coverage caused both by the density of radars and restricted minimum scanning elevation angle occur at many other flood-prone watersheds in the coastal mountains along the West Coast (Westrick et al. 1999). Reynolds (1995) suggested that lowering the minimum scanning elevation to 0° would be required to significantly improve WSR-88D precipitation estimates associated with shallow rain sampled over the West Coast. The detailed microphysical observations necessary to explain the physical mechanisms responsible for this shallow rain process were not undertaken during CALJET. In fact it was only after CALJET that analysis of the data collected during this first-time deployment of S-PROF revealed this rain process and its frequency of occurrence. We begin with descriptions of specific rainfall processes used later to categorize the radar reflectivity and Doppler vertical velocity measurements collected by S-PROF at CZD.

Brightband rain is formed through ice crystal growth and subsequent melting (e.g., Battan 1959; Anagnostou and Kummerow 1997). The process begins in clouds containing both water droplets and ice crystals. The introduction of ice can occur when ice particles fall from higher clouds, when supercooled droplets freeze, or when ice forms directly on ice nuclei. Ice crystals grow preferentially compared to water droplets because the saturation pressure over water is greater than that over ice. As ice particles fall, they may grow further by colliding with supercooled cloud droplets in the cloud, which freeze on the surface of the ice particles, a process known as riming. As ice or snow particles fall through the melting level, they obtain wet surfaces as they begin to melt. This process makes the particles sticky, and aggregation leads to larger particles. Radar reflectivity increases and is positively correlated with Doppler vertical velocity (DVV) in this region because of the increasing particle size. However, radar reflectivity also increases because the dielectric factor is greater for water than for ice (Battan 1973). The region of increasing reflectivity below the melting level defines the upper portion of the radar bright band. As the particles undergo further melting their density increases, which leads to larger fall velocities. Hydrodynamically unstable drops break up into smaller drops. Radar reflectivity decreases and is negatively correlated with DVV in this region because, although the particles are smaller, their fall velocities increase. Radar reflectivity also decreases because of the vertical mass flux divergence resulting from the increased fall velocities, which causes the number concentration to decrease (Atlas 1964). The region of decreasing reflectivity defines the lower portion of the radar bright band. As pointed out by Fabry and Zawadzki (1995), other factors contribute to the shape of the radar bright band: particle growth rate, terminal velocity, particle size distribution, and particle shape and orientation. In this paper we use both radar reflectivity and DVV profiles recorded with the S-PROF at CZD to detect the radar bright band. White et al. (2002) asserted that the use of DVV in addition to radar reflec-

tivity gives added confidence to brightband detection while also allowing for detection when the precipitation does not reach the surface or is too weak to produce a definitive brightband signature in only the radar reflectivity profile. We refer to rainfall that occurs when a radar bright band is detected as BB rain.

Not all rain, however, is accompanied by a bright band. For example, a class of rainfall called warm rain is initiated in clouds with temperatures down to about −15°C, indicating the relative scarcity of ice nuclei compared to cloud condensation nuclei (Whiteman 2000; Rogers and Yau 1989). In warm rain, collision and coalescence allow cloud droplets to grow into raindrops (Zipser and LeMone 1980; Song and Marwitz 1989). This growth process is most efficient when cloud droplets are of different sizes and fall at different speeds. Consequently, warm rain often occurs in coastal regions because of the wide range of aerosol sizes that exists over the oceans (Whiteman 2000). We do not have direct in situ microphysical or cloud-top temperature measurements during CALJET that would allow us to determine unambiguously the presence or absence of ice in the upper regions of precipitating clouds that we expect to be part of a warm rain event. Thus, we do not feel it is appropriate to use the warm rain terminology in this paper. Instead we use the term nonbrightband rain (NBB rain) to indicate a shallow rainfall process which does not produce a detectable bright band, suggesting that ice microphysics does not play a dominant role in the precipitation growth process. We also have ancillary evidence showing that, excluding convection, the NBB rain encountered at CZD often occurred wholly or substantially below the melting level as well as below the lowest beam of the WSR-88D radar situated southeast of San Francisco (KMUX; Fig. 1).[1] The NBB rain referred to here is not to be confused with the NBB or warm rain associated with tropical convection (Szoke and Zipser 1986; Williams et al. 1995; Atlas and Ulbrich 2000) or with the convective cores imbedded in stratiform precipitation often found in midlatitude cyclones (e.g., Smyth and Illingworth 1998). However, as will be shown later, similarities exist between the NBB rain discussed here and the semitropical orographic rain observed in the Hawaiian Islands (e.g., Blanchard 1953).

On some occasions, the BB rain measured by the S-PROF exhibited some of the properties of the NBB rain, namely that the radar reflectivity and DVV magnitude increased below the melting layer. The behavior of the DVV alone suggests further growth by collision and coalescence, since fall speed is inversely proportional to air density (e.g., Foote and duToit 1969). We have labeled this subcategory of BB rain ''hybrid'' rain. It is unclear whether this behavior is simply a manifestation of the seeder–feeder mechanism (Bergeron 1965). In the orographic version of this process precipitation falls from a ''seeder'' cloud, formed by large-scale ascent, into a moisture-rich ''feeder'' cloud, formed by flow over elevated terrain. The orographic enhancement depends on, among other factors, the intensity of seeder precipitation and the speed of the upslope flow. Further details are given by Cotton and Anthes (1989). Another manifestation of the seeder–feeder mechanism is seeder clouds in the form of generating cells, which seed a lower-level feeder cloud produced by frontal ascent. This can result in mesoscale rainbands that propagate in the storm environment (e.g., Rutledge and Hobbs 1983).

The observing systems used in this study are described in section 2. In revealing the structure of NBB rain, we felt it was necessary to describe meteorological conditions under which this rain process occurs. This is our primary motivation for section 3, which uses the case study approach to highlight synoptic environments that contributed to NBB rain events. However, the case study approach does not tell the whole story, because individual cases are chosen, subjectively, based on whether they exhibited a certain behavior. Therefore, in section 4 we use statistical approaches and develop an objective algorithm that determines whether a radar bright band is present in the S-PROF data collected during a specified averaging period. The algorithm then is applied to the 3 months of S-PROF data collected during the CALJET period (January through March 1998) to determine the contribution of NBB rain to the total rainfall observed at the coastal mountain site. Section 5 describes the mean meteorological attributes of NBB rain events and uses wind profiler observations to determine whether orographic forcing contributed to these events, while study conclusions are presented in section 6.

2. Observing systems

a. Ground-based observing network

During CALJET, a ground-based network of specialized meteorological instrumentation was strategically deployed along the California coast to supplement the operational tropospheric observing systems (i.e., the WSR-88D radars and rawinsondes). Together with CALJET's aircraft observations taken offshore, the combined ground-based network provided an invaluable dataset for researchers, weather forecasters, and forecast users during an active winter season. The location of key sites within the ground-based network is shown in Fig. 1. Table 1 lists the instruments and measurements at each site that provided data for, or is mentioned in, this paper.

[1] Only the NWS Doppler radar near Sacramento, California (KDAX), is closer to CZD than KMUX (~133 vs ~198 km, respectively). However, the lowest beam from KDAX in the direction of CZD is blocked by terrain, making KMUX the better choice for NWS precipitation surveillance above CZD.

TABLE 1. Ground-based instrument locations and characteristics for each site that provided data for, or is mentioned in, this paper. All of these sites are located in or near the CALJET orographic processes array (see Fig. 1).

Site	Lat (°N)	Lon (°W)	Height MSL (m)	Instrument	Variables measured or retrieved*	Temporal sampling	Max height or range (km)	Range-gate resolution (m)
Cazadero (CZD)	38.61	123.21	475	3-GHz (S-band) profiler	Z, w	90 s	8.5	100
				915-MHz profiler	v, w, V_r, S	6 min–1 h	4.5	60–100
				RASS	T_v	1 h	1.0	100
				Surface met. package	P, T, T_d, v, r	2 min	—	—
Bodega Bay (BBY)	38.31	123.07	12	915-MHz profiler	v, w, V_r, S	6 min–1 hr	4.5	60–100
				RASS	T_v	1 h	1.0	100
				Surface met. package	P, T, T_d, v, r	2 min	—	—
Oakland (OAK)	37.75	122.22	6	Rawinsonde	P, T, T_d, v	12 h	>16	variable
Mount Umunhum (KMUX)	37.16	121.90	1077	WSR-88D Doppler radar	Z, v, V_r	1–60 min	230	1000
Sacramento (KDAX)	38.50	121.68	9	WSR-88D Doppler radar	Z, v, V_r	1–60 min	230	1000

* Variables measured or retrieved include horizontal wind velocity (v), vertical radial velocity (w), oblique radial velocity (V_r), reflectivity (Z), signal power (S), virtual temperature (T_v), temperature (T), dewpoint temperature (T_d), pressure (P), rainfall (r).

1) VERTICALLY POINTING S-BAND PROFILER AT CAZADERO

The NOAA/ETL vertically pointing S-band profiler or S-PROF is based on the prototype built at the NOAA Aeronomy Laboratory (NOAA/AL; Ecklund et al. 1999). The radar's wavelength of 10 cm is ideally suited for rainfall measurements, though its receiver has a linear dynamic range of only approximately 45 dB, which is not sufficient to cover the full range of reflectivities present in all types of precipitation. Therefore, the S-PROF hardware includes a switchable, 30-dB coupler placed between the radar antenna and the receiver to help extend the dynamic range of the receiver. Further details are given by White et al. (2000).

During CALJET, the S-PROF at Cazadero was programmed to continuously alternate sampling between three modes: a ''coupled mode'' for heavy precipitation, a ''standard mode'' for light to moderate precipitation, and a ''pulse coded'' mode for cloud measurements. Pulse coding provides a means of increasing the average transmitted power without sacrificing range resolution (e.g., Schmidt et al. 1979). The three operating modes used during CALJET are shown schematically in Fig. 2. Details of the profiler calibration are provided by White et al. (2000).

After CALJET, radar reflectivity and DVV measurements from the three operating modes were composited using reflectivity thresholds to determine which operating mode provided the optimal measurement at a particular height. For example, the radar reflectivity measurements from the first eight range gates of the coupled mode are compromised because the received signals are only partially decoded. Therefore, the compositing routine would select standard mode measurements in place of coupled mode measurements for the first eight heights of each composited profile. However, if the reflectivity in the standard mode at a particular height approached the upper limit of its useable reflectivity range as shown in Fig. 2, then the coupled mode would be selected for that particular range gate. We refer to the composited measurements as comprising a ''combined mode.'' By taking advantage of pulse coding and the microwave coupler, the radar reflectivity measurements in the combined mode have a dynamic range of 96 dB (see Fig. 2).

2) INTEGRATED WIND-PROFILER OBSERVING SYSTEMS

The integrated wind-profiler observing system was developed at NOAA/AL and NOAA/ETL and has been an important part of meteorological and climate research since 1990. At the heart of this observing system is a 915-MHz boundary layer wind profiler (Carter et al. 1995). The wind profiler routinely provides hourly averaged vertical profiles of horizontal wind velocity from ~0.1 to 4.0 km above ground with ≤100 m vertical resolution in clear, cloudy, and precipitating conditions. After CALJET, the winds were objectively edited using the vertical–temporal continuity method of Weber et al. (1993), and an extra level of quality control was performed by visual inspection. A radio acoustic sounding system (RASS; May et al. 1989) provided vertical profiles of virtual temperature, which we later transformed into profiles of virtual potential temperature using the method described by Neiman et al. (1992). The upper range of these profiles typically reaches ~500–1000 m above ground.

Wind and temperature data measured by a collocated 10-m surface meteorological tower at each profiler site extended the hourly wind and temperature profiles down to the surface. The tower was also equipped with a tipping-bucket rain gauge that measured rainfall every 2 min with 0.01-in (~0.25 mm) resolution. Surface measurements of wind, temperature, moisture, and pressure were also taken at each site. The meteorological tower data collected during CALJET were postprocessed at NOAA/ETL using an automated quality-control routine designed to remove obvious outliers. The final meteo-

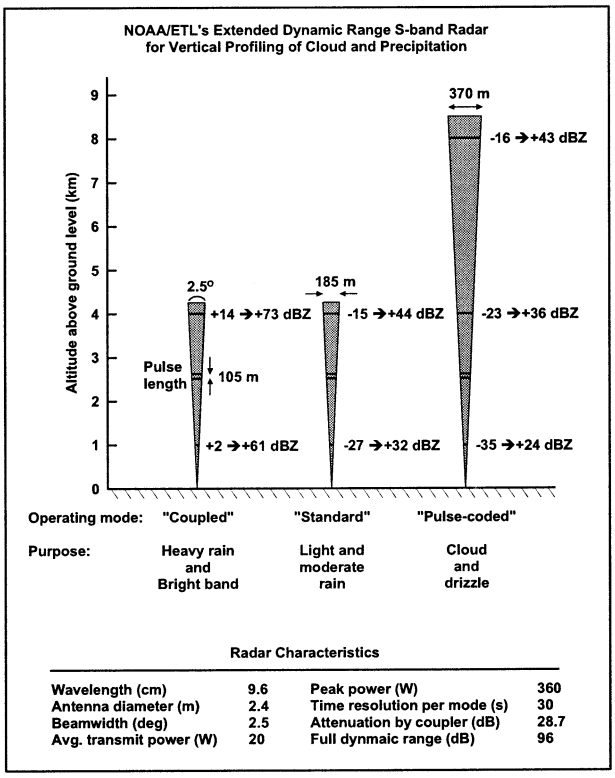

FIG. 2. Characteristics of the NOAA/ETL vertically pointing S-band profiler at Cazadero, and a summary of its three operating modes used during CALJET. Radar sensitivity ranges (dBZ) are indicated at altitudes of 1 and 4 km for all three operating modes and at 8 km for the pulse-coded mode.

rological data products are available at 2-min and hourly resolution.

b. NOAA P-3 research aircraft

A NOAA P-3 turboprop research aircraft measured nearly continuous (1 s) standard navigational and meteorological parameters during 26 CALJET flights between 18 January and 24 March 1998, all of which originated from Monterey, California (location shown in Fig. 1). More than 200 Global Positioning System (GPS) dropsondes were released from the P-3 during the CALJET campaign to obtain high-resolution vertical profiles of wind velocity, temperature, and moisture over the data-sparse Pacific Ocean offshore of California. A helically scanning tail-mounted X-band (~3.2 cm wavelength) radar provided measurements of reflectivity and Doppler motions within precipitation elements. The radar produced alternating fore- and aft-pointing range–height indicator (RHI) or cross-section scans directed ~19.5° fore and aft of a baseline orthogonal to the aircraft heading (e.g., Jorgensen et al. 1996). Though these fore/aft RHIs can be combined into pseudo-dual-Doppler volume renderings of the flow field (e.g., Jorgensen et al. 1996), our study utilizes only the raw RHIs.

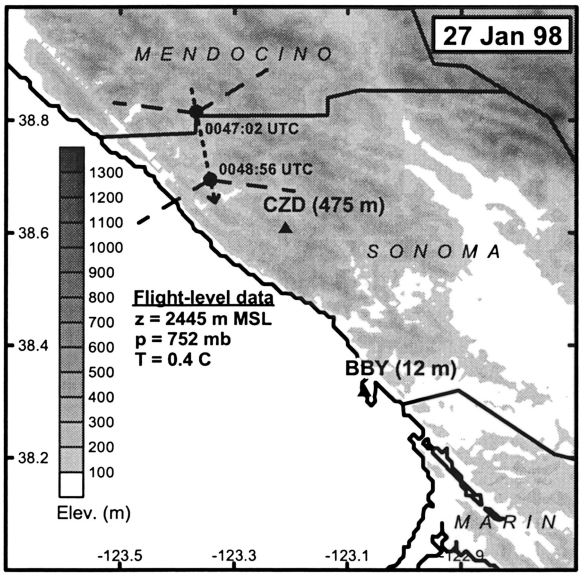

FIG. 3. Terrain base map showing gray-shaded elevations (m), the Cazadero (CZD) and Bodega Bay (BBY) integrated observing sites and their respective elevations (MSL), and projection lines (dashed) of aft- and fore-pointing RHI scans from the P-3 tail radar at 0047:02 and 0048:56 UTC 27 Jan 1998, respectively (see Fig. 4). The relevant southeast-bound P-3 flight track is portrayed as a dotted line, and the time-averaged flight-level data (*z*: altitude; *p*: pressure; *T*: temperature) for this leg are shown. Counties are labeled.

3. Selected nonbrightband rain events and their synoptic environments

Section 1 introduced the vertical-structure characteristics of NBB rain as observed by the S-PROF at CZD. In this section, we utilize a case study approach to describe the vertical–temporal characteristics of NBB rain, and the synoptic conditions in which it occurs.

a. 26–27 January 1998

Early on 27 January 1998, the NOAA P-3 was ideally situated to observe finescale precipitation characteristics over California's coastal mountains near CZD with its tail-mounted Doppler radar (Figs. 3 and 4). An aft-pointing RHI scan of reflectivity at 0047:02 UTC (Fig. 4a) observed a region of rain to the west-northwest of the P-3 that was capped by a well-defined bright band (≥~30 dBZ) approximately 150–200 m beneath the aircraft, or at ~2.3 km above mean sea level (MSL). The brightband location is consistent with the flight-level temperature of 0.4°C. On the opposite (i.e., east-northeast) side of the aircraft, spatially homogeneous and shallow (<~2 km deep) reflectivities ranging between ~5 and 24 dBZ are depicted. This shallow precipitation was, in fact, NBB rain since it was devoid of a bright band and positioned exclusively beneath the melting level. Additional pockets of shallow NBB rain were observed to the west-northwest of the P-3 beyond the BB rain. Less than 2 min later at 0048:56 UTC, a

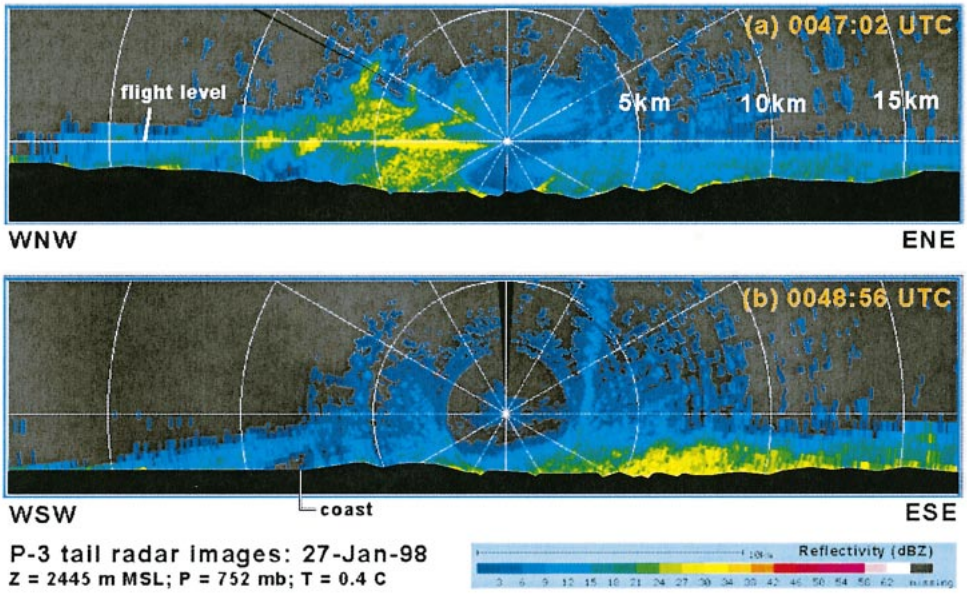

FIG. 4. RHI scans of radar reflectivity (dBZ; scale lower-right) from the P-3 tail radar at (a) 0047:02 UTC, and (b) 0048:56 UTC 27 Jan 1998. Range rings are in 5-km intervals. The flight level is portrayed as a horizontal white line, and the aircraft is located at the center of the range rings. The time-averaged flight-level data are as in Fig. 3.

fore-pointing RHI scan (Fig. 4b) also clearly captured the spatial uniformity and shallow character of the NBB rain hugging the terrain beneath the melting level, which is approximated by the flight level. The NBB rain reflectivities to the east-southeast of the aircraft ranged between 20 and 30 dBZ. It should be noted that the NBB rain east of the P-3 decreased in intensity southward from the southern RHI.

A companion analysis of remote-sensing and surface data from CZD (Fig. 5) provides detailed information of the passage of the relevant frontal features, as well as a comprehensive description of the radar-observed properties of the precipitation. The warm front at the surface moved northward beyond CZD at 0448 UTC 26 January, as evinced by slight veering of the surface flow and the cessation of a 5-h period of nocturnal warming at the surface (Fig. 5d) and aloft (RASS data not shown). Between 0448 and 2340 UTC 26 January, CZD was situated in the warm sector, where the wind profiler observed deep south-to-southwest flow (Fig. 5a), and the surface temperature remained relatively constant (Fig. 5d). The final 6 h of warm-sector conditions were characterized by enhanced deep southerly flow associated with a prefrontal jet. The cold frontal zone passed CZD between 2340 UTC 26 January and 0030 UTC 27 January, during which time the flow in the layer between ~1.5 and 3.0 km MSL shifted clockwise by ~20° to 40° (Fig. 5a), and the alongfront component of the flow in this layer decreased by ~10 m s^{-1}. Terrain-blocked flow (e.g., Parish 1982; Bell and Bosart 1988; Colle and Mass 1995; Overland and Bond 1995; Doyle 1997) below ~1.5 km retarded the frontal wind shift and surface thermodynamic response until after 0115 UTC 27 January. Prior to the warm-frontal passage at the surface (i.e., during warm-frontal conditions), NBB rain totaling 7.3 mm was observed by the S-PROF in the warm-frontal zone until 0400 UTC (Figs. 5b–d). There was no bright band or companion vertical gradient of Doppler vertical velocity observed near the melting level during this period. Between 0448 and 2340 UTC, steady rain fell in the warm sector. The rain exhibited mostly hybrid characteristics (i.e., distinct bright band and associated DVV gradient near the melting level; Figs. 5b,c), though intermittent episodes of NBB rain were also observed. Rainfall increased in intensity leading up to, and during, the cold-frontal passage (Fig. 5d), and it was dominated by hybrid rain characteristics (Figs. 5b,c). Following the passage of the back edge of cold front aloft, only NBB rain fell, and the reflectivities in this shallow precipitation approached 20 dBZ below 1 km MSL (i.e., well beneath the melting level of ~2.5 km MSL). It was during this post-cold-frontal period that the P-3 radar observations of NBB rain were also taken; the magnitude of the reflectivities from the P-3 and S-PROF were similar. Though only a modest amount of NBB rain fell during this post-cold-frontal period (2.8 mm) and the earlier warm-frontal period (7.3 mm), this case was presented because the P-3 was ideally situated to document the spatial distribution of NBB rain that fell, behind the cold front, in the coastal mountains. In contrast, the following two case studies reveal NBB rain events that yielded very significant accumulations in these synoptic environments.

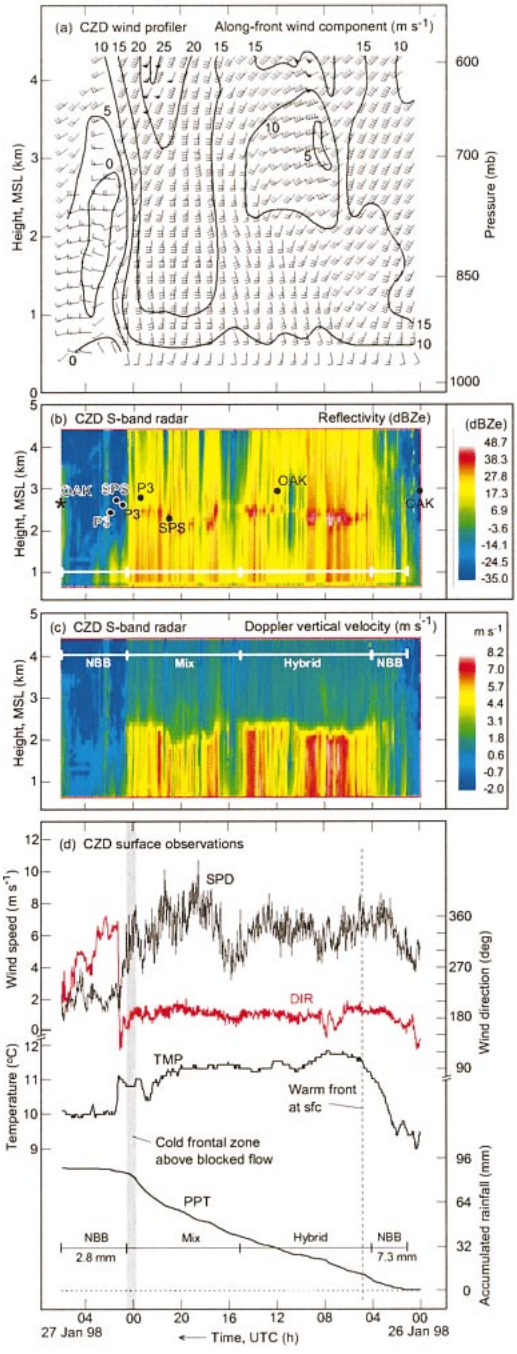

FIG. 5. Time series of data from the Cazadero (CZD) integrated observing site between 0000 UTC 26 Jan and 0600 UTC 27 Jan 1998. (a) Time–height section of wind flags and barbs (flags = 25 m s^{-1}; full barbs = 5 m s^{-1}; half barbs = 2.5 m s^{-1}) and alongfront isotachs (directed from 180°; thin solid) from the 915-MHz wind profiler. Surface winds from CZD are included. (b),(c) Time–height sections of equivalent radar reflectivity factor (dBZ$_e$; i.e., reflectivity) and Doppler vertical velocity (m s^{-1}) from the S-band profiler. Melting-level heights are shown from Oakland rawinsondes (OAK; solid dots are direct measurements, and stars are interpolated measurements from adjacent 12-h soundings), Salt Point airsondes (SPS; located on the coast, west of CZD), and the P-3 aircraft (P3; flight-level data in the vicinity of CZD). (d) Time series traces of surface data [SPD = wind speed (m s^{-1}); DIR = wind direction (deg); TMP = temperature (°C); PPT = accumulated rainfall (mm)]. The vertical dashed line and gray-shaded bar mark relevant frontal passages. The dominant rainfall type periods are shown in (b)–(d), and the two periods of nonbrightband (NBB) rain accumulation are documented in (d). Rainfall type ''mix'' refers to a complex period characterized by NBB rain occurring intermittently with either brightband (BB) and/or hybrid rain.

b. 23–24 March 1998

The event of 23–24 March contained the heaviest episode of NBB rain during CALJET. During this event, a dropsonde-intensive P-3 flight on 23–24 March provided critical observations of relevant weather features over the otherwise data-sparse Pacific Ocean offshore of California (Fig. 6a). A dropsonde-based cross section of θ and alongfront wind at ~0000 UTC 24 March (Fig. 6b; along line AA′ in Fig. 6a) shows the vertical continuity of a cold front extending upward and westward from the ocean surface just offshore of central California to ~400 mb over the open ocean. Strong southwesterly flow was situated on the warm side of the front, while weaker west-southwesterly flow resided on its cold side. Enhanced vertical shear encompassed the frontal zone. Companion infrared satellite imagery (not shown) contained a well-defined comma-cloud tail that tracked southward with this front.

A time–height section of hourly wind profiles and alongfront isotachs from the CZD wind profiler (Fig. 7a) documented the cold-frontal passage between 1600 and ~1720 UTC 23 March above ~1.3 km MSL, though the back edge of the front was ill-defined. The winds between 1.3 and 2.5 km MSL veered with time from south-southwesterly ahead of the front to weaker southwesterly behind, and the strongest alongfront flow was situated immediately ahead of the front. Because a prolonged period of terrain-parallel flow in excess of 10–15 m s^{-1} was observed in the lower troposphere in response to blocked flow in the coastal zone, the front did not penetrate downward to the surface until after 0000 UTC 24 March (Figs. 7a,d). Prior to the cold front's arrival, a mixture of mostly hybrid and NBB rain fell (Figs. 7b–d). The front itself was accompanied by a convective narrow cold-frontal rainband (NCFR) and a trailing region of stratiform hybrid rain that, together, persisted for ~1.6 h. Following a subsequent 20-min lull, NBB rain commenced at 1800 UTC 23 March in the post-cold-frontal environment and continued until 0000 UTC 24 March. During this 6-h period, a total of 53.7 mm of NBB rain fell, accounting for 71% of the rainfall accumulation on this day.

Time–height sections of DVV and equivalent radar reflectivity factor covering the full vertical range of S-PROF's combined mode (see section 2a) are shown in Fig. 8. The added height range reveals the evolving vertical distribution of cloud observed during this event. Early in the period (1000–1400 UTC) two cloud layers

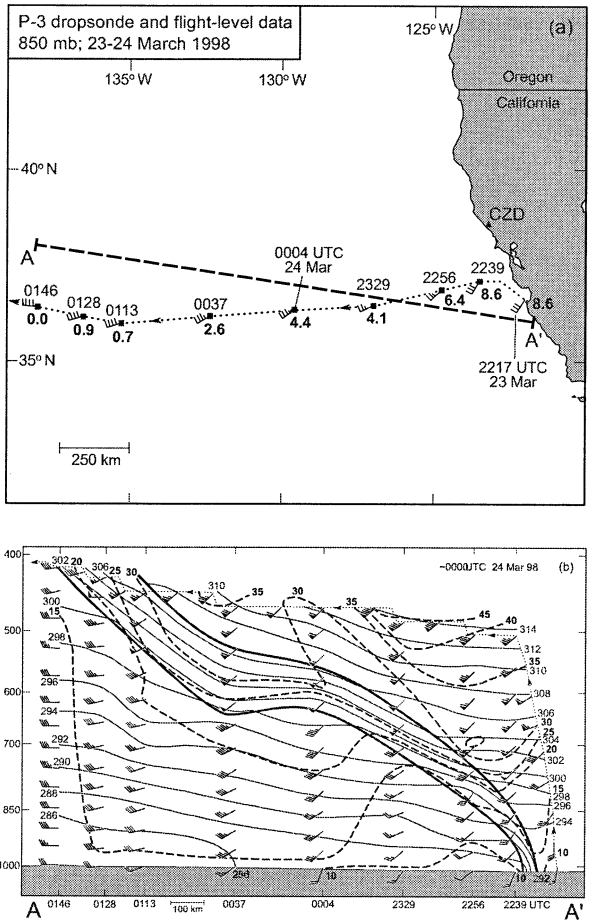

FIG. 6. (a) Base map showing the westbound P-3 flight track (dotted line) and dropsonde deployment locations (bold squares) and times between 2213 UTC 23 Mar and 0153 UTC 24 Mar 1998. The wind flags and barbs (as in Fig. 5) with the square heads are dropsonde observations at 850 mb and the remaining vector is a flight-level observation at 850 mb; companion temperatures (°C) at 850 mb are plotted. The bold dashed line is a projection line for the cross section in (b). (b) Cross section of potential temperature (K, solid) and along-front wind speed directed from 225° (m s^{-1}, dashed) along AA′ of (a) at ~0000 UTC 24 Mar 1998. Bold solid lines are the frontal boundaries. Dropsonde soundings are labeled with times of deployment (UTC). The P-3 flight track is depicted with a thin dotted line. Selected flight-level and dropsonde wind flags and barbs are plotted; flags and barbs are as in Fig. 5.

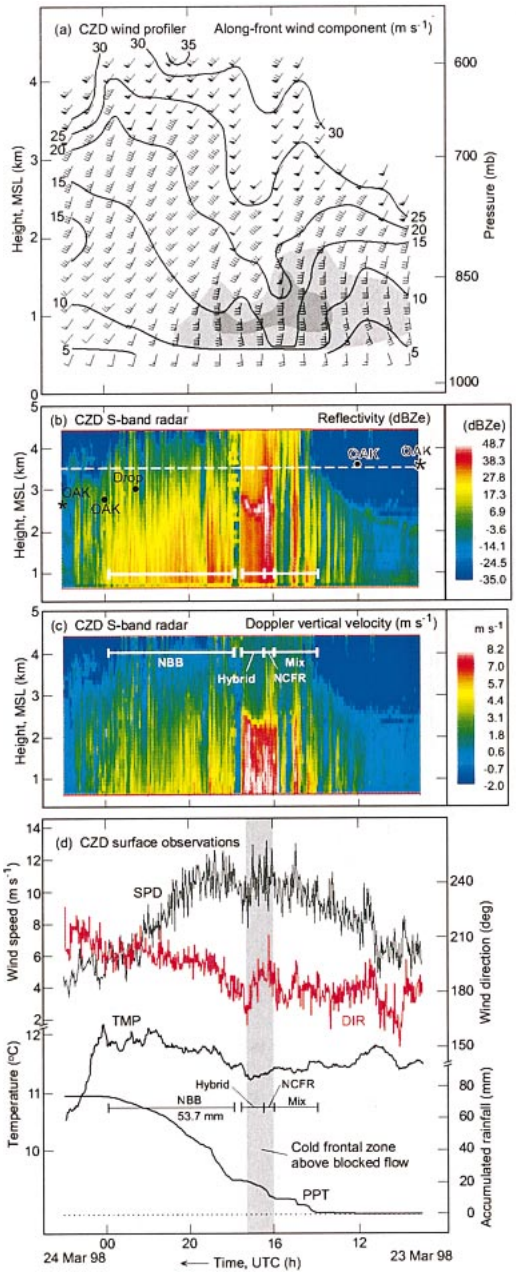

FIG. 7. The same as in Fig. 5, except for the period 0900 UTC 23 Mar to 0200 UTC 24 Mar 1998. The alongfront flow in (a) is directed from 225°. Light and dark shading in (a) portrays terrain-parallel flow (directed from 140°) greater than 10 and 15 m s^{-1}, respectively. The solid dot labeled drop in (b) refers to a P-3 dropsonde observation of the melting level. The white dashed line in (b) denotes the bottom of the ~3.2 km deep beamwidth, over CZD, of the lowest beam (0.5° elev) from the WSR-88D at KMUX. Rainfall type NCFR in (c),(d) refers to the narrow cold-frontal rainband.

were present, but the upper cloud was decoupled from the lower cloud. The lower cloud deepened and was able to sustain light (0.3 mm h^{-1}) precipitation for 2 h. After 1400 UTC the upper and lower cloud layers were coupled, producing heavier rain through the hybrid process. After passage of the cold front and its accompanying NCFR, the upper cloud decoupled again and eventually disappeared by ~1930 UTC. Meanwhile, the NBB rain process ensued. Substantial NBB rain (18.3 mm) was observed during the 1-h period ending 1900 UTC (Fig. 7d), which far surpasses the rule-of-thumb rainrate threshold of 12 mm h^{-1} used by local forecasters for guidance in issuing flood statements. Subsequent hourly NBB rainfall totals of 9.1 and 11.2 mm approached this threshold. These hourly rain rates were the largest of the entire event. Based on the S-PROF and rain gauge observations, it is clear that NBB rain can contribute significantly to individual rain events in

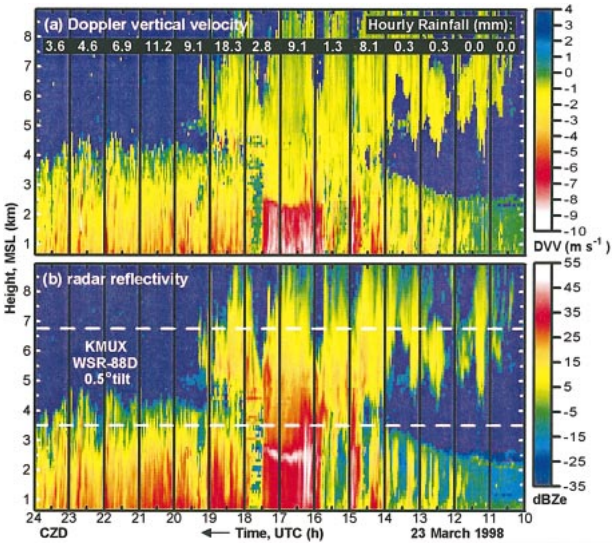

FIG. 8. Time–height sections of (a) Doppler vertical velocity (DVV; m s^{-1}) and (b) equivalent radar reflectivity factor (dBZ_e), recorded by the S-band profiler at CZD for the period 1000 UTC 23 Mar to 0000 UTC 24 Mar 1998. The hourly rainfall accumulations (mm) measured by a tipping-bucket rain gauge collocated with the radar are listed in (a). The horizontal dashed lines denote the ~3.2 km deep beamwidth, over CZD, of the lowest beam (0.5° elevation) from the San Francisco area WSR-88D at KMUX.

the coastal mountains. However, major NBB rain events do not occur solely in post-cold-frontal conditions, as the case from 21 February 1998 will reveal. Significantly, the lowest-angle radar beam from the operational NWS Doppler radar at KMUX scanned almost entirely above the potentially flood-producing NBB rain detected beneath the melting level by the S-PROF at CZD (Fig. 8).

c. 21 February 1998

The second heaviest episode of NBB rain during CALJET occurred in the event of 21 February 1998. Because all transient weather features during this event were well defined, in part because low-level blocking was not significant, the remote-sensing and surface data and analyses from CZD (Fig. 9) provided persuasive evidence to unambiguously diagnose synoptic regimes without using supplemental data sources. The wind-profiler and RASS[2] analyses, and companion surface traces, from CZD (Figs. 9a and 9d) show the descent of a warm front to the surface between 0400 and 1145 UTC 21 February. During this warm-frontal period, the surface flow veered with time from southerly to southwesterly, strong southwesterly component flow (>~20 m s^{-1}) and an axis of maximum thermal-wind-derived warm

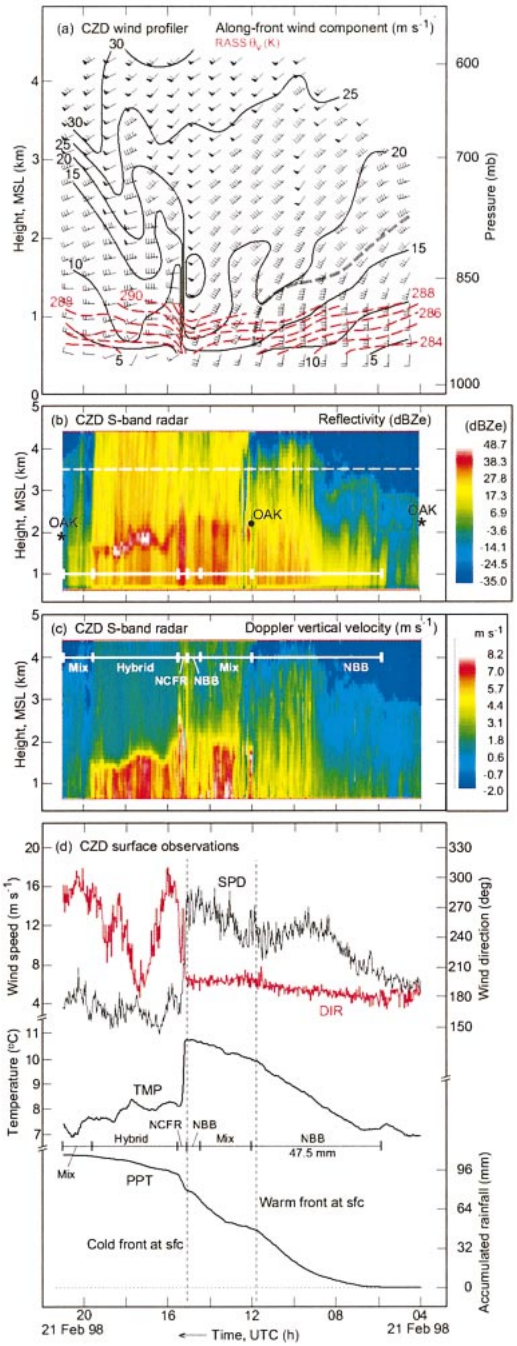

FIG. 9. The same as in Fig. 5 except for the period 0400 to 2100 UTC 21 Feb 1998. (a) Includes the axis of max thermal-wind-derived warm advection (gray-shaded dashed line), and an analysis of RASS virtual potential temperature (red dashed; K). The alongfront flow in (a) is directed from 225°. The white dashed line in (b) is as in Fig. 7. Rainfall type NCFR in (c),(d) refers to the narrow cold-frontal rainband.

advection (i.e., clockwise turning of the wind direction with increasing height) descended toward the surface from aloft, the temperature in the lowest ~750 m increased by ~3 K, and nearly one-half of the total rain

[2] RASS analyses for the previous two events were not shown, because blocked flow during those events extended above the RASS measurements. Hence, in those cases, RASS could not provide useful information on the transient frontal features aloft.

for this event fell. Between 1145 and 1505 UTC warm-sector conditions prevailed, characterized by warm (10°–11°C) and strong (12–25 m s^{-1}) southwesterly flow at the surface and aloft, and significant rainfall. The leading edge of a sharp cold front raced across CZD at 1505 UTC, accompanied by a burst of heavy rain, an abrupt wind shift in the lower troposphere from strong southwesterly to weaker westerly flow, and a sharp 2.5–3.0-K decrease in temperature in the lowest ~750 m. A layer of enhanced vertical wind shear associated with the cold front ascended to ~3 km MSL by 2100 UTC 21 February.

Based on the S-PROF observations at CZD (Figs. 9b,c), exclusively NBB rain fell prior to the warm-frontal passage at the surface at 1145 UTC. A total of 47.5 mm NBB rain fell during this warm-frontal period and at the onset of warm-sector conditions (Fig. 9d). The rain rate ranged between 10 and 13 mm h^{-1} for three consecutive 1-h periods between 0900 and 1200 UTC, thus highlighting the fact that NBB rain can contribute to heavy rainfall during warm-frontal, as well as during post-cold-frontal, episodes. As was the case during the previously described NBB rain event on 23–24 March, the heavy NBB rain on 21 February was situated beneath the lowest-angle NWS Doppler radar beam from KMUX and largely beneath the melting level (Fig. 9b). Within the warm sector, a mixture of rain types was observed (Figs. 9b,c). The subsequent cold-frontal passage was accompanied by a convective NCFR and trailing region of stratiform hybrid rain.

4. S-PROF statistical analyses

a. Rainfall process partitioning

An objective algorithm was developed to estimate the contribution of each rainfall process (i.e., NBB, BB, and hybrid) to the total rainfall observed at CZD during the CALJET period (1 January–31 March 1998). We chose a 30-min averaging period for the radar and accumulation period for the rain gauge. This period is long enough to provide an adequate number of samples to apply statistical methods. The 30-min window contains 15 rain gauge measurements and ~20 radar profiles. Analysis was performed on all half-hour periods when the rain rate exceeded ~1 mm h^{-1}. Because the bucket in the gauge is designed to tip with every 0.01 in (0.254 mm) of accumulation, this rain-rate threshold corresponds to a requirement of two tips in the half-hour period.

Within the periods satisfying the rain-rate threshold, the rainfall process partitioning algorithm (RPPA) selects only those radar profiles where the equivalent radar reflectivity factor in the lowest range gate is at least 10 dBZ_e, to make it more likely that the profile was obtained in rain and to avoid including gaps in the precipitation. A test is then applied on each of these profiles to determine if a bright band is present. For this test,

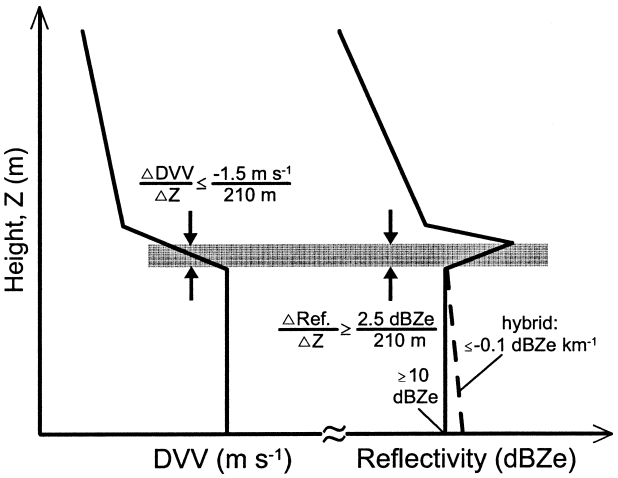

FIG. 10. Schematic showing the criteria used to partition brightband rain and nonbrightband rain. Indicated are the magnitudes of the jumps (denoted by Δs) in Doppler vertical velocity (DVV; positive downward) and equivalent radar reflectivity factor (i.e., reflectivity) that were employed to objectively detect the lower portion of the bright band. An additional criterion is shown that was used to further partition the hybrid portion of the brightband rain (dashed line).

the RPPA searches for the lower portion of the bright band, where the DVV magnitude decreases with height and the radar reflectivity increases with height. If an increase of at least 2.5 dBZ_e in radar reflectivity and a decrease of at least 1.5 m s^{-1} in DVV magnitude occur over an altitude span of 210 m (i.e., two radar range gates), the profile is determined to contain a bright band (Fig. 10). White et al. (2002) developed a similar method for deducing the brightband height from radar reflectivity and DVV measurements taken with the commercially available 915-MHz wind profilers. If the percentage of profiles containing a bright band in the half-hour meets or exceeds 50%, the rainfall is ascribed to BB rain. Otherwise, the NBB rain process is designated.

The RPPA uses the slope of reflectivity below the melting layer as the criterion for distinguishing between BB rain and its subcategory of hybrid rain. For the results presented here, we chose a slope of -0.1 dBZ_e km^{-1} to be the threshold at which the hybrid process is designated (i.e., a slope ≤ -0.1 dBZ_e km^{-1} indicates hybrid rain). In other words, we assume that any growth of the raindrops reflected in a positive downward increase in reflectivity below the melting layer indicates the hybrid process. Regardless, the partitioning of NBB rain does not involve this parameter and, thus, is not affected by this assumption. Figure 10 summarizes the criteria used in the RPPA.

In convective rain, the classic brightband structure is often not visible because of enhanced turbulence, or the presence of graupel or hail, even though convective rain clouds may extend well above the melting level. This is especially true in the NCFR. We used the unaveraged S-PROF, wind profiler, and surface meteorology data collected during each half-hour period ascribed to NBB

TABLE 2. Results of a rainfall process partitioning algorithm applied to half-hourly periods of rainfall observed at CZD during CALJET (1 Jan–31 Mar 1998).

Rain process	Rainfall (mm)	Time (h)
Brightband rain (BB rain)	292 (16%)	84.0 (15%)
Hybrid rain	805 (44%)	162.0 (29%)
Nonbrightband rain (NBB rain)	647 (35%)*	166.0 (29%)
Rain rate <1 mm h^{-1}	76 (4%)	149.5 (27%)
Missing radar data	21 (1%)	2.5 ($\sim$0%)
Dry	0	1596.0
Totals	1841	564/2160** (26%)

* Total for all NBB rain events including 134 mm of convective rain. Excluding the convective rain, the NBB rain contribution would be 513 mm or 28% of total rainfall observed.

** The fraction of half-hour periods when rainfall was observed by the CZD rain gauge.

rain by the RPPA to subjectively evaluate whether or not the rain was associated with convection. We did not attempt to do this objectively for two reasons. First, the convective rain associated with the NCFRs, which accounted for most of the convective rainfall that occurred during the 3-month period, was easily diagnosed by visual inspection with support from the aforementioned datasets. Second, it was not obvious how to develop an objective algorithm to remove all convective rainfall, because the precipitation that fell in the cold sector was often weakly convective but shallow enough to be considered NBB rain. The rare events when the melting layer fell below the minimum detectable range of the radar were attributed to BB rain.

Results of the RPPA are listed in Table 2. Close to half (44%) of the rainfall was attributed to the hybrid process. We believe this could be an indication of the prevalence of the seeder–feeder mechanism contributing to the orographic rainfall observed at CZD. On the other hand, NBB rain contributed significantly (28% after excluding convective rainfall) to the winter season total, and, although this process resulted in a slightly lower average hourly rainfall rate than the other processes, we have shown that NBB rain could cause rain rates exceeding the 12 mm h^{-1} rule-of-thumb threshold used by forecasters for guidance in issuing flood statements (see Fig. 7).

A histogram of rainfall intensity for the 564 h (1841 mm) of rainfall that fell at CZD during the period 1 January through 31 March, 1998 is shown in Fig. 11a. Here, all half-hour periods of rainfall are included. Light rain was observed with the greatest frequency, similar to what has been observed at many other locations. The percentage of time that each rainfall process occurred at a given rainfall intensity is shown in Fig. 11b. Because the RPPA excluded cases with rain rates <1 mm h^{-1}, there is no information available for the first rainfall-rate bin. Bars corresponding to rainfall rates with less than eight half-hour data points (i.e., 4 h in Fig. 11a) are also not shown. Rainfall determined to be convective in nature was not included in the NBB rain bars (see Table 2). NBB rain was slightly favored for the lower rainfall rates but contributed as strongly to the higher rainfall rates as well. Curiously, neither NBB rain nor BB rain occurred when the measured rainfall rate was in the range of 12–13 mm h^{-1}.

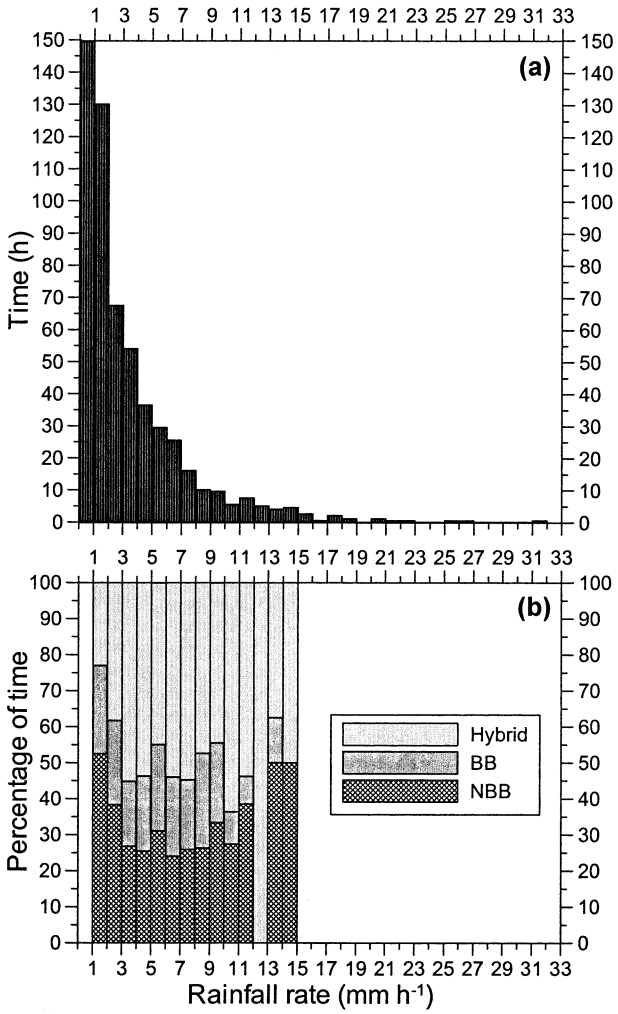

FIG. 11. (a) Histogram of rainfall intensity measured at CZD during the period Jan–Mar 1998. The rainfall rates are based on 30-min accumulations measured by a tipping-bucket rain gauge. (b) The percentage of time that each rainfall process occurred for a given rainfall intensity. The rainfall process breakdown is not shown for rain rates exceeding 15 mm h^{-1} because of the limited data availability at the heaviest rain rates, and it is not shown for rain rates $<$ 1 mm h^{-1} because the process partitioning technique requires rain rates of at least 1 mm h^{-1}.

Prominent differences in the vertical structure of BB and NBB rain are evident in Fig. 12, which compares profiles of radar reflectivity and DVV measured in periods of light and heavy rainfall. The large differences in the values of radar reflectivity and DVV measured near the surface in periods of BB and NBB rain that produced very similar rain rates indicate variance in the drop-size distributions (DSDs) associated with each

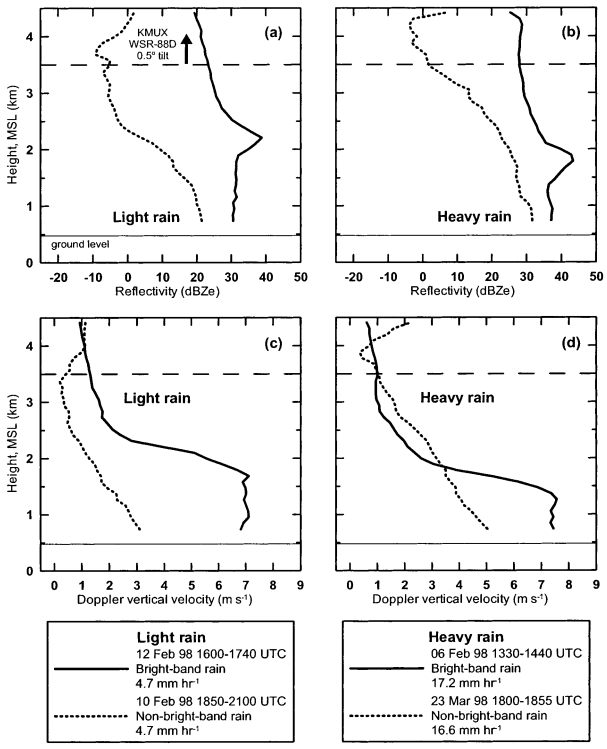

FIG. 12. Vertical profiles of equivalent radar reflectivity factor (dBZ_e) measured with the NOAA/ETL S-band profiler for (a) a period of light brightband rain (4.7 mm h^{-1}; solid) and nonbrightband rain (4.7 mm h^{-1}; dotted), and (b) a period of heavy brightband rain (17.2 mm h^{-1}; solid) and nonbrightband rain (16.6 mm h^{-1}; dotted). The companion vertical profiles of Doppler vertical velocity (m s^{-1}; positive downward) for the same periods are also shown: (c) light rain and (d) heavy rain. The date, averaging time window, rain type, and rain rate for each sample period are shown in the keys below. The horizontal dashed lines in (a)–(d) denote the bottom of the ~3.2 km deep beamwidth, over CZD, of the lowest beam (0.5° elevation) from the WSR-88D at KMUX. The horizontal solid lines mark ground level.

rainfall process. These limited comparisons support the hypothesis that NBB rain contains a higher concentration of small drops than BB rain. The next section investigates whether this hypothesis applies on a statistical basis to all BB and NBB rain events observed during CALJET.

b. Vertical profile statistics

Using the results of the RPPA, we produced contoured frequency-by-altitude diagrams, or CFADs (see appendix A in Yuter and Houze 1995) from the winter season S-PROF dataset to compare the bulk physical properties of BB and NBB rain in a statistical manner. Because our intent here is to identify the characteristic structures of rainfall observed when a BB is or is not present, we combined BB rain and hybrid rain into a single category and denoted this category as BB/hybrid rain. Figure 13 shows CFADs of DVV and radar reflectivity for BB/hybrid rain and NBB rain. To help separate the radar data for this purpose, we included half-hour periods in the CFAD analysis if at least 80% of the profiles obtained within the half-hour indicated BB/hybrid rain or NBB rain. Approximately 2% of the heavier BB/hybrid rain events were not included to allow the average rain rate to be the same for both sets of CFADs. For BB/hybrid rain (Figs. 13a,b), the height of individual profiles was adjusted so that the range gate where the BB peak in radar reflectivity occurred was closest to the average BB height (BBH) for the entire winter season. This explains why the relative frequency of profiles used in the BB/hybrid CFADs drops off below 1.6 km MSL (Fig. 13c).

The relative frequency of profiles used in the NBB CFADs begins to drop off significantly above 2.4 km (Fig. 13f) because the radar reflectivities measured in NBB rain above the melting level (approximated by the inferred BBH in Figs. 13d,e) were often too small to be detected with S-PROF operating in its most sensitive pulse-coded mode (see Fig. 2). The large spread in the distribution of radar reflectivity and DVV in this region aloft occurs (Figs. 13d,e) because sky conditions above the NBB rain varied from clear to overcast over the course of the winter season. When two or more cloud layers were present, the upper layer(s) were decoupled from the NBB rain cloud layer; that is, there was no indication of precipitation falling out of the upper cloud layer(s). The upper portion of the velocity CFAD for NBB rain (Fig. 13d) shows slightly positive modal DVVs, indicating the presence of small ice particles in some of the deeper NBB cases. However, the modal DVV does not increase with decreasing height above the inferred BBH for the NBB rain, suggesting that the growth of the NBB raindrops is primarily a warm process.

The spread in DVV and radar reflectivity at the lowest gate of the CFADs for BB/hybrid and NBB rain (Figs. 13a,d) result from the distribution of rainfall intensities observed over the course of the winter season. Yet, the modal velocity at the lowest gate in NBB rain is only 2.25 m s^{-1} compared to 6.25 m s^{-1} for BB/hybrid rain, even though the average rainfall rate is the same in both cases. In BB/hybrid rain, the effect of the variation in rainfall intensity near the surface is not reflected above the freezing level because of the narrow range of fall velocities exhibited by snowflakes, which is indicated by the narrow distributions of DVV above the BBH (Fig. 13a). The spread of the distributions of radar reflectivity remains fairly uniform in height for BB/hybrid rain (Fig. 13b). The modal radar reflectivity at the lowest gate of the BB/hybrid rain is 28.5 dBZ_e compared to 20.5 dBZ_e for the NBB rain, despite the fact that both radar reflectivity distributions produced the same average rainfall rate. Blanchard (1953) found that orographic rains observed in Hawaii with intensities greater than 10 mm h^{-1} had radar reflectivities that were 4 to 10 dBZ_e lower than the radar reflectivity measured in nonorographic (i.e., thunderstorm type) rains. The

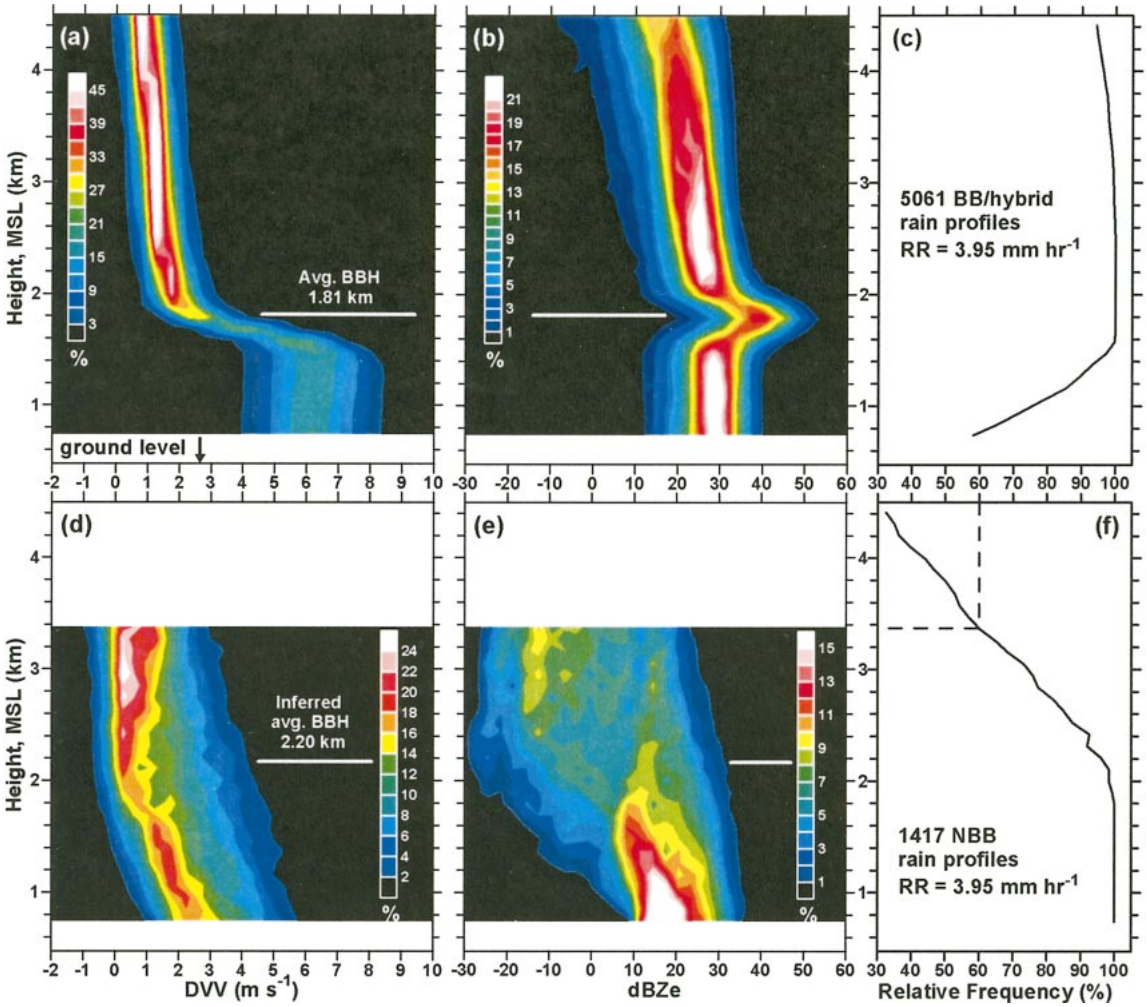

FIG. 13. Contoured frequency-by-altitude diagrams, or CFADs, produced from profiles of Doppler vertical velocity (DVV; m s^{-1}) and equivalent radar reflectivity factor (dBZ_e) collected in rain with the S-band profiler at CZD during CALJET (Jan–Mar 1998). Colored contours display the frequency of occurrence relative to the total number of observations available at a particular height. The DVV bin size is 0.5 m s^{-1} and the radar reflectivity bin size is 3 dBZ_e, (a),(b) Brightband (BB) rain. The height of each BB rain profile was adjusted in 105-m increments so that the bright band occurred at the range-gate height closest to the average brightband height (BBH) for the entire winter season (indicated by the white lines). (d),(e) Nonbrightband (NBB) rain. The average BBH for NBB rain was inferred from brightband rain profiles, when available, recorded immediately before or after a NBB rain period. Roughly 2% of the BB rain profiles obtained in heavier rain events were excluded from the analysis in order to produce the same average rainfall rate (3.95 mm h^{-1}) for the BB and NBB CFADs. (c),(f) The percentage of profiles available at each range gate relative to the total number of profiles listed for BB rain and NBB rain, respectively. The NBB CFADs are shown for all range gates where the relative frequency exceeds 60%.

marked differences in the bulk physical properties of NBB and BB/hybrid rain evidenced by these results further demonstrate that the NBB and BB/hybrid rain observed in this study were composed of substantially different DSDs.

These results also suggest that the NBB rainfall process would be misrepresented in rainfall estimates derived from satellite. Passive microwave techniques that map brightness temperatures to rainfall rate (e.g., Wilheit et al. 1977) likely would underestimate NBB rain because of the relatively warm cloud-top temperatures of the shallow NBB rain clouds. Techniques involving satellite precipitation radars (e.g., Schumacher and Houze 2000) must assume a DSD to relate radar reflectivity to rainfall rate. Applying a DSD that is not applicable to the NBB rain also would yield inaccurate satellite rainfall estimates.

c. *Reflectivity–rain-rate relationships*

Another way of comparing the bulk physical properties of BB/hybrid and NBB rain in a statistical manner is to compute reflectivity–rain-rate (Z–R) relationships for each rainfall process. By doing so, we are not advocating Z–R as a diagnostic tool, although historically this method has been used for quantitative precipitation

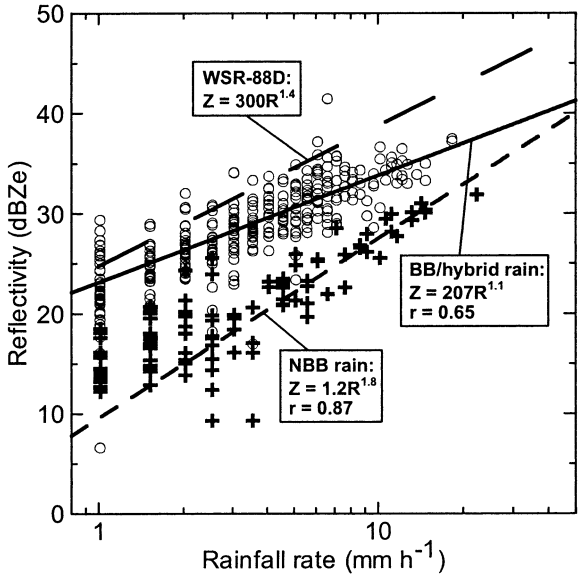

FIG. 14. Scatterplot of radar reflectivity at 273 m AGL vs rain rate for NBB rain (plus symbols) and BB/hybrid rain (open circles). The lines denote the linear (in log space) regression fits for NBB rain (short dashed) and BB rain (solid), excluding rainfall rates < 3 mm h^{-1}. The default *Z–R* relationship used with the WSR-88D is indicated by the long-dashed line. The correlation coefficient, *r*, is listed for the regression fits to BB rain and NBB rain.

estimation (QPE) with the WSR-88D network. Here, our intention is to provide a means of summarizing the different characteristics of BB/hybrid and NBB rain. Scatterplots of *Z–R* for the half-hour periods used to establish the CFADs, including the heavier BB rain periods that were not included in the BB CFADs in order to match rainfall rates, are shown in Fig. 14, along with the default *Z–R* relationship used for QPE with the WSR-88D network. The reflectivity data are from 263 m AGL, the height of the lowest useable range gate from S-PROF in its CALJET configuration. The *Z–R* relationships for BB/hybrid and NBB rain were calculated from linear (in log space) regression fits. We excluded rain rates less than 3 mm h^{-1} to prevent the scatter associated with the numerous light rain events from influencing the slopes of the regression fits. The NBB rain is characterized by a steeper slope than either the BB/hybrid rain or the WSR-88D default. However, for the range of half-hourly rainfall rates observed, the NBB radar reflectivities are consistently less than the BB/hybrid reflectivities, which was also evident in Fig. 13. The *Z–R* coefficient for NBB rain is two orders of magnitude less than the coefficient for BB rain and the WSR-88D relationship. Blanchard (1953) reported on the *Z–R* coefficient for Hawaiian orographic rains and found that it was one to two orders of magnitude lower than the coefficient for other types of rain. The correlation coefficient for NBB rain (0.87) is substantially greater than the correlation coefficient for BB/hybrid rain (0.65), perhaps because of the increased variability of the DSDs in BB/hybrid rain introduced by ice microphysics.

5. Orographic forcing during NBB rain

Though the S-PROF observations during CALJET were limited to a single winter season that experienced record rainfall during a prominent warm phase (i.e., El Niño phase) of the El Niño–Southern Oscillation (ENSO), they may provide clues as to why shallow NBB rain is most likely to occur in California's coastal mountains. Using a subset of the objectively tagged NBB rainfall that was deemed nonconvective, we will now briefly explore the connection between orographic forcing and NBB rain by examining composited and individual hourly wind profiles associated with both NBB rain and all significant rain events that occurred during the CALJET winter season.

To determine the mean wind conditions at CZD during the significant rain events for the CALJET winter season, we first examined the rainfall database from late November 1997 through March 1998 and chose events at CZD that exceeded 12.5-mm rainfall and 8-h duration. A total of 33 cases spanning 602 h fit these criteria. This winter-season inventory captured 88% of the 2158 mm of rain that fell during this ~100 day period (not shown). Then, by averaging the hourly wind profiles measured by the 915-MHz profiler at CZD during these 602 h, we constructed mean winter-season profiles of wind speed, wind direction, and the components of the flow perpendicular and parallel to the mean mountain-barrier orientation (directed from 230° and 140°, respectively). We also constructed mean wind profiles using hourly wind-profiler measurements taken during NBB rain episodes. To ensure that an hourly wind profile properly represented conditions associated with NBB rain, at least 80% of the rain observed by the S-PROF for that hour was required to exhibit NBB characteristics (based on the rainfall partitioning analysis). Using this stringent definition, a total of 38 1-h periods contained NBB rain (Table 3), though considerably more than 38 h of NBB rain fell during the 3-month S-PROF deployment (Table 2).

The mean wind speed and direction profiles from the NBB and winter-season inventories are shown in Fig. 15. Though the speed profiles are quite similar above 1.75 km MSL, only the NBB profile exhibits a weak low-level jet (LLJ), which is centered at 1.25 km MSL. A study of the impact of the low-level jet on orographic precipitation by Neiman et al. (2002) defined the LLJ as a maximum of total wind speed below 1.5 km MSL residing beneath a local minimum aloft. To meet the LLJ criteria, the maximum was required to be at least 2 m s^{-1} greater than the minimum aloft. The composite wind speed profile for NBB rain does not satisfy the second criterion. The LLJ is centered at 1.25 km MSL, but the maximum is only 0.48 m s^{-1} greater than the minimum aloft. Of the 38 individual profiles in the NBB

TABLE 3. Data inventory for those 1-h periods of rainfall at CZD that contained at least 80% NBB rain.[a]

Case	NBB rain period (1997–98)[b]	Duration (h)	CZD rainfall (mm)	CZD rain rate (mm h^{-1})	BBY rainfall (mm)	BBY rain rate (mm h^{-1})	Rainfall ratio (CZD/BBY)
1	0700 UTC 2 Jan–1000 UTC 2 Jan	3	18.54	6.18	2.54	0.85	7.30
2	1900 UTC 2 Jan–2100 UTC 2 Jan	2	5.33	2.67	0.51	0.26	10.45
3	0100 UTC 3 Jan–0200 UTC 3 Jan	1	3.30	3.30	0.00	0.00	—
4	0700 UTC 10 Jan–0800 UTC 10 Jan	1	1.52	1.52	6.27	6.27	0.24
5	0900 UTC 10 Jan–1000 UTC 10 Jan	1	5.33	5.33	0.76	0.76	7.01
6	0200 UTC 12 Jan–0500 UTC 12 Jan	3	10.16	3.39	3.75	1.25	2.71
7	0600 UTC 12 Jan–0700 UTC 12 Jan	1	1.29	1.29	0.00	0.00	—
8	0900 UTC 12 Jan–1000 UTC 12 Jan	1	2.79	2.79	0.25	0.25	11.16
9	0900 UTC 14 Jan–1000 UTC 14 Jan	1	1.02	1.02	0.00	0.00	—
10	0900 UTC 15 Jan–1000 UTC 15 Jan	1	1.79	1.79	0.25	0.25	7.16
11	2300 UTC 23 Jan–0000 UTC 24 Jan	1	3.56	3.56	1.02	1.02	3.49
12	0100 UTC 24 Jan–0300 UTC 24 Jan	2	3.81	1.91	0.00	0.00	—
13	0100 UTC 26 Jan–0300 UTC 26 Jan	2	4.06	2.03	0.51	0.26	7.96
14	0100 UTC 27 Jan–0200 UTC 27 Jan	1	1.78	1.78	0.00	0.00	—
15	0300 UTC 29 Jan–0400 UTC 29 Jan	1	1.78	1.78	0.00	0.00	—
16	1500 UTC 31 Jan–1600 UTC 31 Jan	1	1.27	1.27	0.00	0.00	—
17	1600 UTC 1 Feb–1700 UTC 1 Feb	1	6.10	6.10	6.10	6.10	1.00
18	1900 UTC 10 Feb–2100 UTC 10 Feb	2	9.40	4.70	11.62	5.81	0.81
19	1900 UTC 12 Feb–2000 UTC 12 Feb	1	1.78	1.78	1.52	1.52	1.17
20	0700 UTC 21 Feb–1200 UTC 21 Feb	5	46.23	9.25	5.25	1.05	8.81
21	1800 UTC 23 Mar–0000 UTC 24 Mar	6	54.09	9.02	6.01	1.00	9.00
NBB rain totals		38	184.93		46.36		
NBB rain avg				4.87		1.22	3.99
33-case winter season rain avg[c]				3.14		1.45	2.21

[a] The fractional occurrence of NBB rain in each 1-h period was determined by applying the objective rainfall partitioning algorithm to the vertically pointing S-PROF data. The S-PROF operated at CZD between 1 Jan and 31 Mar 1998.

[b] The two date–time stamps for each entry correspond to the start and end dates and times. The format of the date–time stamps is as follows: time (UTC), day, month.

[c] The winter season at this site is defined as 20 Nov 1997 to 31 Mar 1998. Events less than 12.5 mm total rainfall and less than 8-h duration were excluded from this winter-season rainfall inventory. A total of 602 h of data are included in this inventory.

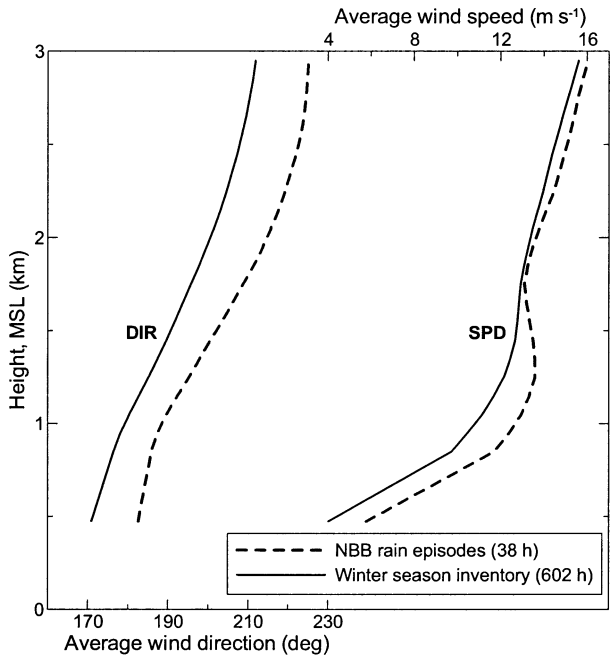

FIG. 15. Composite profiles of wind direction (DIR; deg) and wind speed (SPD; m s^{-1}) based on data from the 38-h NBB rain inventory (dashed) and the 602-h winter-season rainfall inventory (solid).

composite, 79% contain an LLJ below 1.5 km MSL and 40% of those, or 32% of the total, satisfy the jet-strength criterion. Nevertheless, the composite LLJ associated with NBB rain is 1.5 to 2.0 m s^{-1} stronger than the composite flow based on the winter-season inventory. The mean wind direction for NBB events is rotated 10°–15° clockwise relative to the winter-season profile. Significantly, the direction of flow is much more restrictive during NBB rain than during all rain events, especially below 1.5 km MSL (standard deviation of 26.1° versus 40.3°, respectively; not shown). The terrain-perpendicular or upslope component of the flow (not shown) is larger by 1.5–2.5 m s^{-1} during NBB rain, with the largest offset of nearly 30% occurring at the altitude of the composite LLJ. The enhanced upslope flow at low levels, which was a direct result of the weak LLJ at 1.25 km MSL, quite likely contributed to the generation of NBB rain via orographic forcing, as we will now describe.

A comparison of rainfall totals of the NBB and winter-season inventories in the coastal mountains at CZD, and immediately upstream along the coast at Bodega Bay, California (BBY; Table 3), provides clear documentation of substantial rainfall enhancement at CZD, especially during NBB conditions. Specifically, the average rainfall ratio between CZD and BBY during the

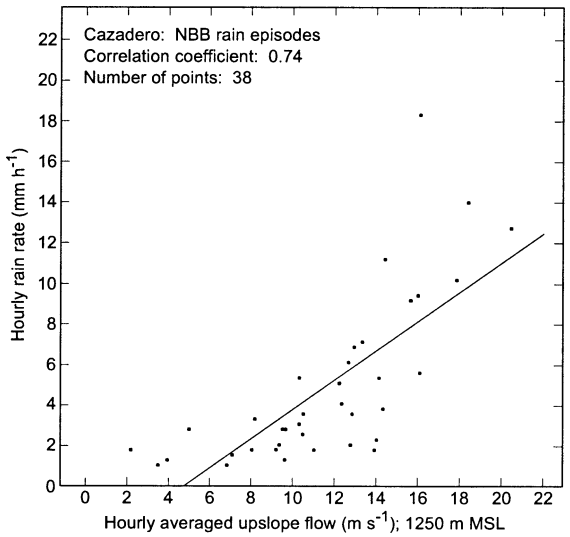

FIG. 16. Scatterplot of hourly averaged upslope flow (at 1250 m MSL) vs hourly rain at CZD during NBB rain episodes. The linear regression fit is shown. The upslope component of the flow is directed toward 50°.

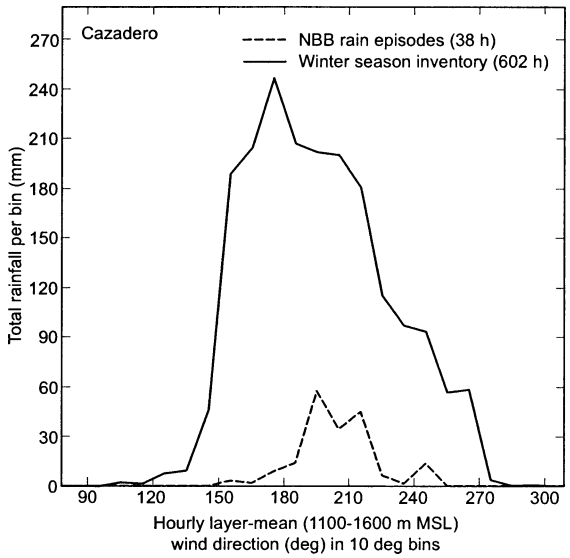

FIG. 17. Hourly averaged wind direction (at 1250 m MSL) vs total rainfall at CZD based on data from the 38-h NBB rain inventory (dashed) and the 602-h winter-season rainfall inventory (solid). The rainfall data were placed in 10° wind-direction bins.

NBB rain events is 3.99:1, whereas the rainfall ratio during the winter-season inventory is only 2.21:1. This 80% increase in rainfall ratio during NBB rain reveals the importance of orographic forcing in these conditions. To quantify the impact of orographic forcing on rainfall, we statistically examined the linear relationship between upslope flow and rain rate at CZD for the 38 h of NBB rain data, and also for the 602 h of rainfall data that make up the winter-season inventory. We derived a correlation coefficient of upslope flow versus rain rate at each range gate (and at the surface) for each data inventory by employing the same technique as described in Neiman et al. (2002). Figure 16 shows a scatterplot diagram of upslope flow at 1250 m MSL (i.e., at the height of maximum correlation coefficient and the low-level jet) versus NBB rain rate. The linear regression fit yields a correlation coefficient of 0.74. In contrast, the correlation coefficient at the same level derived from the 602-h inventory is only 0.52. Alternately stated, 54% of the rain-rate variation was attributed to linear changes in the magnitude of the upslope flow for NBB conditions, whereas this value decreased substantially to 27% for the winter-season rainfall, thus highlighting the added importance of orographic forcing during NBB rain.

In an attempt to discover the flow directions that yield the heaviest rainfall for each of the two rain inventories, we segmented the rainfall as a function of wind direction at the level of maximum correlation (i.e., at 1250 m MSL). Using the 38 h (602 h) of data from the NBB (winter season) inventory at CZD, each hourly rain measurement was placed into a preassigned 10° wind-direction bin based on the simultaneously observed wind direction. The accumulated results are displayed in Fig. 17. The NBB rain occurred within a much narrower wind-direction range than did the winter-season rainfall. In fact, 74% of the NBB rain occurred when the direction of flow at 1250 m MSL ranged between 190° and 220°. In addition, the heavier NBB rain events occurred with low-level wind directions that were more upslope-oriented than during the bulk of the winter-season rainfall events. Since the results in Fig. 17 are based on a statistical analysis during only a single winter season characterized by a strong El Niño episode, it might be premature to use low-level wind direction as a predictive tool for nowcasting NBB rain in California's coastal mountains. Ultimately, a comparable analysis based on multiple years of winter-season data over a wide range of ENSO conditions is required before these research results can be applied definitively by the forecasting community.

6. Conclusions

a. Summary and discussion

This paper used radar reflectivity and Doppler vertical velocity measurements from a vertically pointing S-band radar (S-PROF) to document a shallow, orographic, quasi-steady, NBB rain process and compared this structure to what is found in the much more well-documented BB rain. The distinctively different patterns of radar reflectivity and Doppler vertical velocity associated with each rainfall process were revealed. A schematic that characterizes the statistical behavior of the radar profiles in BB/hybrid and NBB rain for the same rain rate is shown in Fig. 18a. NBB rain consistently occurred with weaker radar reflectivity and smaller

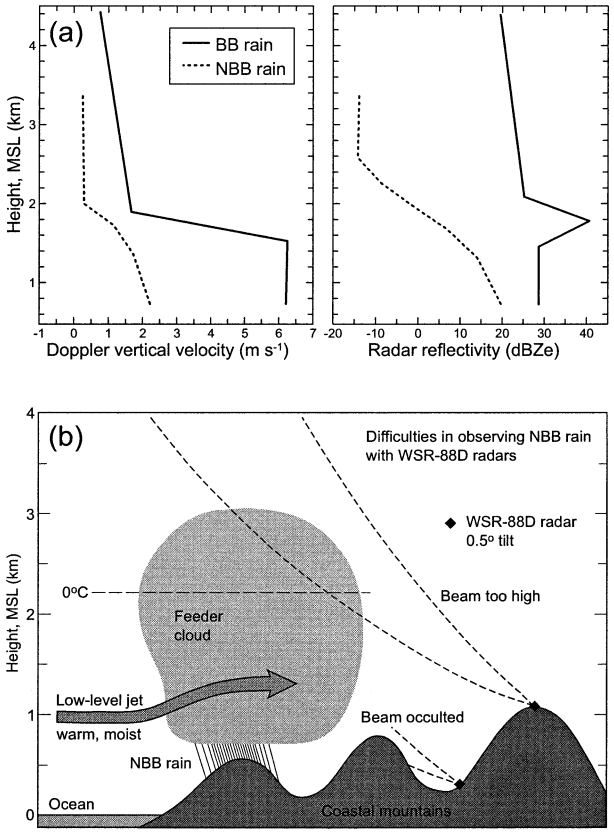

FIG. 18. (a) Composite winter-season profiles of (left) Doppler vertical velocity (m s^{-1}; positive downward) and (right) equivalent radar reflectivity factor (dBZ_e) measured by the S-band profiler during brightband rain (BB; solid) and nonbrightband rain (NBB; dashed). The altitude scale of individual brightband profiles was normalized with respect to the brightband height prior to the compositing, and the composite brightband profiles were then plotted relative to the average brightband height. The average rain rate for each rain type is approximately the same (3.95 mm h^{-1}). These profiles were obtained from Fig. 14. (b) Conceptual representation of shallow NBB rain in California's coastal mountains, and the inability of the operational WSR-88D radars to adequately observe it. NBB rain is portrayed falling from a shallow feeder cloud forced by warm and moist onshore flow associated with a land-falling low-level jet (bold arrow).

Doppler vertical velocity than BB rain for rainfall events that produced nearly equivalent rain rates, implying that NBB rain consists of smaller drops. Unfortunately, direct measurements of the drop-size distributions were not available in this study. Excluding convection, NBB rain accounted for more than one-quarter of the total rainfall (i.e., 512 of 1841 mm) observed at a coastal mountain site during CALJET (1 January–31 March 1998).

In all BB situations, ice crystals must be present above the melting level. However, without in situ sampling or polarimetric radar observations, we could not identify the phase of hydrometeors above the 0°C isotherm in the NBB cases. There may have been supercooled water drops alone, but it is possible also that small ice crystals were present. It seems unlikely, however, that large aggregates of crystals (snowflakes) were involved, because the aggregation process and the large water-coated surface area of melting snowflakes both contribute strongly to producing BB profiles. Falling dendrite crystals are especially efficient at producing large aggregates. In the NBB periods shown in the case studies and in the CFAD statistical analysis, the echo tops were relatively low ($<\sim$3 km MSL) and probably did not reach the -15°C level where dendritic ice crystal growth flourishes. Thus, these NBB rain periods were less likely to have significant aggregation occurring than the BB rain periods when echo tops were considerably higher and colder.

The difficulty of observing NBB rain with the National Weather Service WSR-88D network is shown conceptually in Fig. 18b. Poor radar coverage of rainfall in the coastal mountains of the western United States is a result of the limited density of radars within the network, the restricted minimum scanning elevation angle, and complex topography. The S-band radar deployed at Cazadero during CALJET has elucidated the problem. However, these vertically directed instruments provide information only above one point, and it might require dozens of them to act as an adequate gap-filling supplement to the WSR-88D network in California alone. By allowing the existing WSR-88D radars to scan with elevation angles less than the current minimum limit of 0.5°, some of the coastal gap problem may be alleviated, depending on topographic blocking geometries. Adding new WSR-88D radars to the network, carefully sited near the coastline would be a good, but expensive, solution. Using less expensive, and perhaps shorter wavelength, scanning radars along the coastline is another possible way to fill these gaps. These radars could be less sophisticated than the WSR-88D and devoted solely to monitoring storms approaching from the sea and ascending the mountains at vulnerable watershed locations.

An examination of NBB rain observed by S-PROF during three cases yielded crucial information about its vertical–temporal characteristics, and on synoptic conditions in which it occurs. These radar signatures of NBB rain were largely temporally continuous, often persisting for multiple hours, and they did not contain large vertical undulations. The continuous, rather than intermittent, vertical–temporal character of NBB rain suggests strongly that this class of shallow rain is nonconvective. Airborne radar observations of NBB rain during one of these cases support this assertion. Though most NBB rain is light ($<\sim$5 mm h^{-1}), we observed episodes where it contributed significantly to individual rain events in California's coastal mountains. For example, two of the case studies contained substantial NBB rain rates ranging between 12 and 18 mm h^{-1}, which surpasses the rule-of-thumb rain-rate threshold of 12 mm h^{-1} used by local forecasters for guidance in issuing flood statements. During the three case studies, contin-

uous NBB rain accompanied two different post-cold-frontal regimes with shallow blocked flow, and continuous NBB rain also occurred during the descent of two different warm fronts toward the surface. These synoptic and blocked regimes are typically accompanied by shallow stable stratification. Hence, our results suggest that shallow stably stratified flows may produce conditions favorable for the generation of NBB rain over California's coastal mountains. Unfortunately, we did not have routine measurements of the stratification through a sufficiently deep layer in the vicinity of S-PROF during CALJET.

A CALJET winter-season composite analysis of wind-profiler data taken during all significant rain events, and during NBB rain episodes, provided additional documentation of the meteorological conditions associated with NBB rain in California's coastal mountains. NBB rain was accompanied by stronger (1.5–2.0 m s^{-1}) and more prominent low-level jet conditions at ~1 km MSL than during all rain events. The direction of the incoming flow during NBB rain was 10°–15° more orthogonal to the mountain barrier than during all rain events. In addition, the low-level wind direction was much more restrictive during NBB rain. In fact, three-quarters of the NBB rain fell when the layer-mean wind direction at the height of the composite low-level jet ranged between 190° and 220°.

A comparison of rainfall totals in the coastal mountains, and immediately upstream along the coast, provided clear documentation of substantial orographic rainfall enhancement in the coastal mountains during NBB conditions. To quantify the impact of orographic forcing on rainfall, we statistically examined the linear relationship between upslope flow and rain rate (technique described in Neiman et al. 2002) in the coastal mountains during NBB episodes and during all significant rain events of CALJET. The maximum linear correlation between upslope flow and rain rate at the altitude of the low-level jet (~1.25 km MSL) was 0.74 for NBB rain episodes and only 0.54 for rainfall during the entire winter season, thus highlighting the added importance of orographic forcing during NBB rain.

b. Future work

Using various datasets collected during CALJET, this paper documented the existence of NBB rain, the unique bulk physical attributes of NBB rain relative to its brightband counterpart, the significant contribution of NBB rain to individual rain events and to the winter-season rainfall total, synoptic regimes that support NBB rain, and a physical connection between orographic forcing and NBB rain. Nevertheless, significant gaps in our understanding of NBB rain remain, though these gaps can be bridged in the future with additional observations.

The combination of polarimetric radar, in situ aircraft, and ground-based disdrometer observations could provide information about the detailed microphysical characteristics of NBB rain, including the phase of hydrometeors above the melting level. In addition, serial rawinsonde observations could measure the low-level conditions (i.e., stable stratification, potential instability, moisture flux) that contribute to generating NBB rain. Knowledge gleaned from these new observations can ultimately be applied operationally by improving forecasting of shallow rain events in the coastal zone and by revising reflectivity-based quantitative precipitation estimation algorithms that take into account DSDs associated with NBB rain.

The reflectivity characteristics and Z–R relationships for the NBB rain shown in this paper were consistent with the results found in a study of semitropical orographic rains (Blanchard 1953), perhaps indicating a climate–weather connection between El Niño and the NBB rain observed along the California coast during CALJET. To understand the climatological significance of NBB rain, it will be necessary to obtain the aforementioned datasets at other coastal mountain locations and over the course of other winter seasons that are influenced by different phases of ENSO.

Acknowledgments. This research was supported by the NOAA U.S. Weather Research Program. The authors wish to thank the organizations and scientists who contributed to the success of CALJET and PACJET. We thank, in particular, the Naval Postgraduate School in Monterey, California, for serving as an excellent host and base of operations during CALJET. Special thanks are given to Clark King and the rest of NOAA/ETL's talented field team for deploying and maintaining the wind-profiler network, to Cat Russell for processing the rain gauge and other surface meteorological measurements taken from these sites, and to Dan Gottas for meticulously processing the wind-profiler data. We thank Brooks Martner for many enlightening discussions about radar meteorology and precipitation microphysics. The critical comments provided by three anonymous reviewers led to substantial improvements in this manuscript. We acknowledge David Jorgensen and John Daugherty of NOAA/NSSL for providing tail radar data from the NOAA P-3 aircraft. We thank Robert Mann for allowing us to install the S-band radar and supporting instrumentation on his ranch above Cazadero, California, and the University of California at Davis's Bodega Marine Laboratory in Bodega Bay, for allowing us to install equipment at Bodega Head. Jim Adams provided exceptional drafting services.

REFERENCES

Anagnostou, E. N., and C. Kummerow, 1997: Stratiform and convective classification of rainfall using SSM/I 85-GHz brightness temperature observations. *J. Atmos. Oceanic Technol.,* **14,** 570–575.

Atlas, D., 1964: Advances in radar meteorology. *Advances in Geophysics.* Vol. 10, Academic Press, 317–478.

——, and C. W. Ulbrich, 2000: An observationally based conceptual model of warm oceanic convective rain in the Tropics. *J. Appl. Meteor.,* **39,** 2165–2181.
Battan, L. J., 1959: *Radar Meteorology.* University of Chicago Press, 161 pp.
——, 1973: *Radar Observations of the Atmosphere.* University of Chicago Press, 279 pp.
Bell, G. D., and L. F. Bosart, 1988: Appalachian cold-air damming. *Mon. Wea. Rev.,* **116,** 137–161.
Bergeron, T., 1965: On the low-level redistribution of atmospheric water caused by orography. *Proc. Int. Conf. on Cloud Physics*, Tokyo, Japan, IAMAP/WMO, 96–100.
Blanchard, D. C., 1953: Raindrop size-distribution in Hawaiian rains. *J. Meteor.,* **10,** 457–473.
Carter, D. A., K. S. Gage, W. L. Ecklund, W. M. Angevine, P. E. Johnston, A. C. Riddle, J. S. Wilson, and C. R. Williams, 1995: Developments in UHF lower tropospheric wind profiling at NOAA's Aeronomy Laboratory. *Radio Sci.,* **30,** 997–1001.
Colle, B. A., and C. F. Mass, 1995: The structure and evolution of cold surges east of the Rocky Mountains. *Mon. Wea. Rev.,* **123,** 2577–2610.
Cotton, W. R., and R. A. Anthes, 1989: *Storm and Cloud Dynamics.* Academic Press, 880 pp.
Doyle, J. D., 1997: The influence of mesoscale orography on a coastal jet and rainband. *Mon. Wea. Rev.,* **125,** 1465–1488.
Ecklund, W. L., C. R. Williams, P. E. Johnston, and K. S. Gage, 1999: A 3-GHz profiler for precipitating cloud studies. *J. Atmos. Oceanic Technol.,* **16,** 309–322.
Fabry, F., and I. Zawadzki, 1995: Long-term radar observations of the melting layer of precipitation and their interpretation. *J. Atmos. Sci.,* **52,** 838–851.
Foote, G. B., and P. S. duToit, 1969: Terminal velocity of raindrops aloft. *J. Appl. Meteor.,* **8,** 249–253.
Jorgensen, D. P., T. Matejka, and J. D. DuGranrut, 1996: Multi-beam techniques for deriving wind fields from airborne Doppler radars. *J. Meteor. Atmos. Phys.,* **59,** 83–104.
May, P. T., K. P. Moran, and R. G. Strauch, 1989: The accuracy of RASS temperature profiles. *J. Appl. Meteor.,* **28,** 1329–1335.
Neiman, P. J., P. T. May, and M. A. Shapiro, 1992: Radio acoustic sounding system (RASS) and wind profiler observations of lower- and middle-tropospheric weather systems. *Mon. Wea. Rev.,* **120,** 2298–2313.
——, F. M. Ralph, A. B. White, D. E. Kingsmill, and P. O. G. Persson, 2002: The statistical relationship between upslope flow and rainfall in California's coastal mountains: Observations during CALJET. *Mon. Wea. Rev.,* **130,** 1468–1492.
Overland, J. E., and N. A. Bond, 1995: Observations and scale analysis of coastal wind jets. *Mon. Wea. Rev.,* **123,** 2934–2941.
Parish, T. R., 1982: Barrier winds along the Sierra Nevada Mountains. *J. Appl. Meteor.,* **21,** 925–930.
Ralph, F. M., and Coauthors, 1998: The use of tropospheric profiling in the California Land Falling Jets Experiment (CALJET). *Proc. Fourth Int. Symp. on Tropospheric Profiling: Needs and Technologies,* Aspen, CO, University of Colorado, 258–260.
Reynolds, D. W., 1995: Warm rain process and WSR-88D. Western Region Tech. Attachment 95–08, 7 pp. [Available from NWS Western Region Headquarters, Federal Building, Salt Lake City, UT 84138.]
Rogers, R. R., and M. K. Yau, 1989: *A Short Course in Cloud Physics.* Pergamon Press, 293 pp.
Rutledge, S. A., and P. V. Hobbs, 1983: The mesoscale and microscale structure and organization of clouds and precipitation in midlatitude cyclones. VIII: A model for the ''seeder-feeder'' process in warm-frontal rainbands. *J. Atmos. Sci.,* **40,** 1185–1206.
Schmidt, G., R. Rüster, and P. Czechowsky, 1979: Complementary code and digital filtering for detection of weak VHF radar signals from the mesosphere. *IEEE Trans. Geosci. Electron.,* **GE-17,** 262–280.
Schumacher, C., and R. A. Houze Jr., 2000: Comparison of radar data from the TRMM satellite and Kwajalein oceanic validation site. *J. Appl. Meteor.,* **39,** 2151–2164.
Smyth, T. J., and A. J. Illingworth, 1998: Radar estimates of rainfall rates at the ground in bright band and non-bright band events. *Quart. J. Roy. Meteor. Soc.,* **124,** 2417–2434.
Song, N., and J. Marwitz, 1989: A numerical study of the warm rain process in orographic clouds. *J. Atmos. Sci.,* **46,** 3479–3486.
Szoke, E. J., and E. J. Zipser, 1986: A radar study of convective cells in GATE. Part II: Life cycle of convective cells. *J. Atmos. Sci.,* **43,** 199–218.
Weber, B. L., D. B. Wuertz, D. C. Welsh, and R. McPeek, 1993: Quality controls for profiler measurements of winds and RASS temperatures. *J. Atmos. Oceanic Technol.,* **10,** 452–464.
Westrick, K. J., C. F. Mass, and B. A. Colle, 1999: The limitations of the WSR-88D radar network for quantitative precipitation measurement over the coastal western United States. *Bull. Amer. Meteor. Soc.,* **80,** 2289–2298.
White, A. B., J. R. Jordan, B. E. Martner, F. M. Ralph, and B. W. Bartram, 2000: Extending the dynamic range of an S-band radar for cloud and precipitation studies. *J. Atmos. Oceanic Technol.,* **17,** 1226–1234.
——, D. J. Gottas, E. T. Strem, F. M. Ralph, and P. J. Neiman, 2002: An automated brightband height detection algorithm for use with Doppler radar spectral moments. *J. Atmos. Oceanic Technol.,* **19,** 687–697.
Whiteman, C. D., 2000: *Mountain Meteorology: Fundamentals and Applications.* Oxford University Press, 355 pp.
Wilheit, T. T., A. T. C. Chang, M. S. V. Rao, E. B. Rodgers, and J. S. Theon, 1977: A satellite technique for quantitatively mapping rainfall rates over the oceans. *J. Appl. Meteor.,* **16,** 551–560.
Williams, C. R., W. L. Ecklund, and K. S. Gage, 1995: Classification of precipitating clouds in the Tropics using 915-MHz wind profilers. *J. Atmos. Oceanic Technol.,* **12,** 996–1012.
Yuter, S. E., and R. A. Houze Jr., 1995: Three-dimensional kinematic and microphysical evolution of Florida cumulonimbus. Part II: Frequency distributions of vertical velocity, reflectivity, and differential reflectivity. *Mon. Wea. Rev.,* **123,** 1941–1963.
Zipser, E. J., and M. A. LeMone, 1980: Cumulonimbus vertical velocity events in GATE. Part II: Synthesis and model core structure. *J. Atmos. Sci.,* **37,** 2458–2469.